Photorelease of Nitric Oxide (NO) in Mono- and Bimetallic Ruthenium Nitrosyl Complexes: A Photokinetic Investigation with a Two-Step Model

Yael Juarez-Martinez, Pablo Labra-Vázquez, Pascal Lacroix, Marine Tassé, Sonia Mallet-Ladeira, Véronique Pimienta, Isabelle Malfant

Photorelease of Nitric Oxide (NO) in Mono- and Bi-metallic Ruthenium Nitrosyl Complexes. A Photokinetic Investigation with a Two-step Model

Yael Juarez-Martinez[a], Pablo Labra-Vázquez[a], Pascal G. Lacroix[a]*, Marine Tassé[a], Sonia Mallet-Ladeira[a,b], Véronique Pimienta[c]*, Isabelle Malfant[a]*

a Laboratoire de Chimie de Coordination du CNRS, 205 route de Narbonne, F-31077 Toulouse, France
b Institut de Chimie de Toulouse (ICT, UAR 2599), 118 Route de Narbonne, 31062 Toulouse Cedex 09, France
c Laboratoire SOFTMAT, Université Toulouse III, 118 Rte de Narbonne, 31062 Toulouse, France

ABSTRACT: Two monometallic and three bimetallic ruthenium acetonitrile (RuMeCN) complexes are presented and fully characterized. All of them are built from the same skeleton $[FTRu(bpy)(MeCN)]^{2+}$, in which FT is a fluorenyl-substituted terpyridine ligand, and bpy the 2,2'-bipyridine. The crystal structure of $[FTRu(bpy)(MeCN)](PF_6)_2$ is presented. A careful spectroscopic analysis allows establishing that these 5 RuMeCN complexes can be identified as the product of the photoreaction of 5 related RuNO complexes, investigated as efficient nitric oxide (NO) donors. Based on this set of complexes, the mechanism of the NO photorelease of the bimetallic complexes has been established through a complete investigation under irradiations performed at 365, 400, 455, and 490 nm wavelength. A two-step ($A \rightarrow B \rightarrow C$) kinetics model specially designed for this purpose provides a good description of the mechanism, with quantum yields of photorelease in the range 0.001 – 0.029, depending on the irradiation wavelength. In the first step of releases, the quantum yields (ϕ_{AB}) are always found to be larger than those of the second step (ϕ_{BC}), at any irradiation wavelengths.

1. INTRODUCTION

Nitric oxide (NO•) has gradually been recognized to play a major role in numerous physiological functions, such as neurotransmission, blood pressure regulation, stimulation of immune response and cytotoxic activity in tumor cells by apoptosis.[1-6] Therefore, exogenous NO• donors have been intensively investigated for various therapeutic applications.[7] Among them, ruthenium nitrosyl (RuNO) complexes appear especially appealing due to their generally low toxicity, good stability in biological medium, and furthermore their capability to release NO• under light irradiation in the λ = 300-500 nm domain, exclusively, taking advantage of the non-invasive and highly controllable characteristics of light.[8-12] However, and to be fully applicable, the NO• photo-release should be achieved in the λ = 600 – 1 300 nm therapeutic window of relative transparency of biological tissues.[13]

To overpass this difficulty, our group has been engaged in a research effort aiming at designing RuNO chromophores capable to release NO• by means of the two-photon absorption (TPA) technique. TPA, which replaces one photon in the visible domain by two photons in the therapeutic window, has gained

widespread popularity in the biology community and has become an extremely powerful tool for local photo-activation and drug delivery.[14,15] Along this line, we have recently reported on a series of five complexes (**RuNO-1** to **RuNO-5** in Chart 1), comprised by several bimetallic species with enhanced TPA response (cross-section parameter σ_{TPA}).[16,17] Investigating bimetallic systems leads to the possibility to have an access to centro- or pseudo-centrosymmetric geometries, which have been reported to provide chromophores of higher σ_{TPA} values than those of the related dipolar geometries, both theoretically,[18] and experimentally.[19]

In monometallic RuNO complexes, the NO• release is well described as arising from an initial electronic absorption having strong charge transfer character toward the strongly withdrawing [Ru-(NO)] fragment, which leads to a substitution of NO by a molecule of solvent,[9,16,20,21] as described below:

$$[Ru(NO)] + solvent \xrightarrow{h\nu} [Ru(solvent)] + NO^{\bullet} \quad (1)$$

However, the NO• photorelease from bimetallic species rises the issue of the afferent mechanism, either in one or two steps, according to the following equations:

$$\underset{A}{[Ru(NO)Ru(NO)]} + solvent \xrightarrow{h\nu} \underset{C}{[Ru(solvent)Ru(solvent)]} + 2\ NO^{\bullet} \quad (2)$$

$$\underset{A}{[Ru(NO)Ru(NO)]} + solvent \xrightarrow{h\nu} \underset{B}{[Ru(NO)Ru(solvent)]} + NO^{\bullet} \quad (3a)$$

$$\underset{B}{[Ru(NO)Ru(solvent)]} + solvent \xrightarrow{h\nu} \underset{C}{[Ru(solvent)Ru(solvent)]} + NO^{\bullet} \quad (3b)$$

Although it seems natural to consider a route in two steps ($A \rightarrow B \rightarrow C$, equations 3a and 3b), a first report of photo-kinetic behavior on these species[16] revealed the presence of apparent isosbestic points in the UV-visible spectra all over the NO• release process in agreement with a simple one-step ($A \rightarrow C$, equation 2) description of the mechanism.

The present contribution is an attempt to fully elucidate this issue, and to provide a complete understanding of the NO• release in bimetallic complexes. In our investigation, acetonitrile (MeCN) is used as the solvent, in any case. The organization of the manuscript is as follows: (*i*) we report first the chemical synthesis of the five **RuMeCN-1** to **RuMeCN-5** complexes related to the five **RuNO-1** to **RuNO-5** in which the [Ru-(NO)] fragments are replaced by [Ru-(MeCN)], together with that of the so-

called [**Ru(NO)Ru(MeCN)]-5** bimetallic species, hypothetical intermediate in the NO• photorelease from **RuNO-5**. (*ii*) their UV-visible spectra are then presented to establish precisely the spectroscopic signature of the photoproduct of **RuNO-5**. (*iii*) Finally, the mechanism of the release in the bimetallic species is addressed with the help of a two-step model specially designed for the purpose of this investigation.

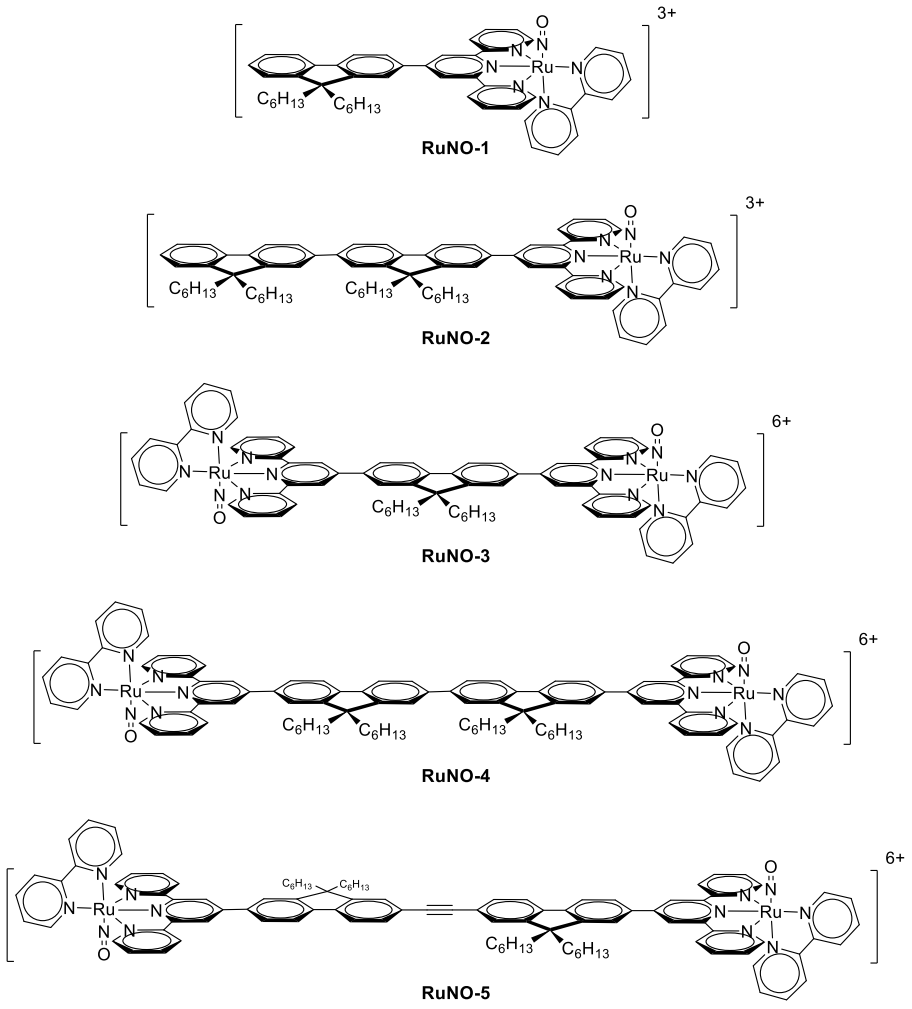

Chart 1 Ruthenium complexes under investigation. Reproduced with permission from Juarez-Martinez, Y.; Labra-Vázquez, P.; Enríquez-Cabrera, A.; Leon-Rojas, A. F.; Martínez-Bourget, D.; Lacroix, P. G.; Tassé, M.; Mallet-Ladeira, S.; Farfán, N.; Santillan, R.; Ramos-Ortiz, G.; Malval, J.-P.; Malfant, I. Bimetallic Ruthenium Nitrosyl Complexes with Enhanced Two-Photon Absorption Properties for Nitric Oxide Delivery. Chem. Eur. J. 2022, 28, e202201692 (1-14). Copyright Wiley-VCH GmbH.

2. RESULTS AND DISCUSSION

2.1. Synthesis and characterization

*Synthesis of **RuMeCN-1,5***

The five **RuMeCN-1,5** complexes related to the five **RuNO-1,5** complexes (Chart 1) in which the nitrosyl ligands are replaced by acetonitrile were synthetized by chemical procedures to be compared with the analogous materials obtained by irradiation of **RuNO-1,5**, but never isolated.[16] Both approaches are compared in Scheme 1. Details for the synthetic procedures and characterizations are provided in *Supporting Information*.

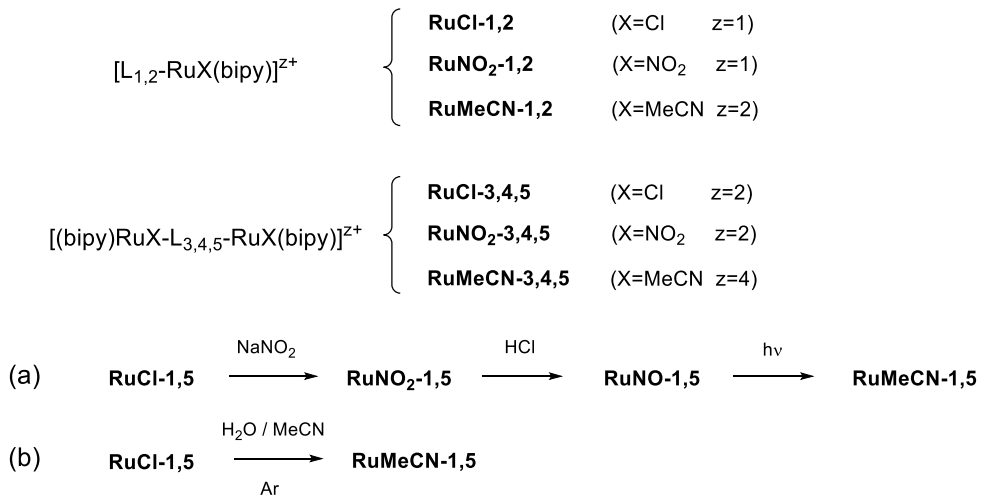

Scheme 1. The routes towards **RuMeCN-1,5**. (a) photochemical option where the chlorido present in [Ru(terpy)(bipy)Cl] is replaced by NO_2, NO, and finally MeCN after $NO^{\bullet}$ photorelease ; (b) chemical synthesis (this contribution) where the chlorido is directly replaced by MeCN.

To improve solubility, two hexyl chains are grafted on the fluorenylterpyridine ligands in the **RuMeCN-1,5** series, which hampered our numerous attempts to get single crystals suitable for X-ray structure determination. Nevertheless, a crystal structure was obtained for a non-alkylated version of **RuMeCN-1**, namely [**RuMeCN-1**'](PF$_6$)$_2$, the asymmetric unit of which is shown in Figure 1. The presence of two PF_6^- anions leads to the conclusion that the ruthenium atom is in the +II oxidation state, as were all the different [Ru(terpy)(bipy)X] complexes investigated in our team.[21] Two molecules of acetone, solvent used for the crystallization, are present in the asymmetric unit. Details can be found in *Supporting Information* (CCDC 2310622).

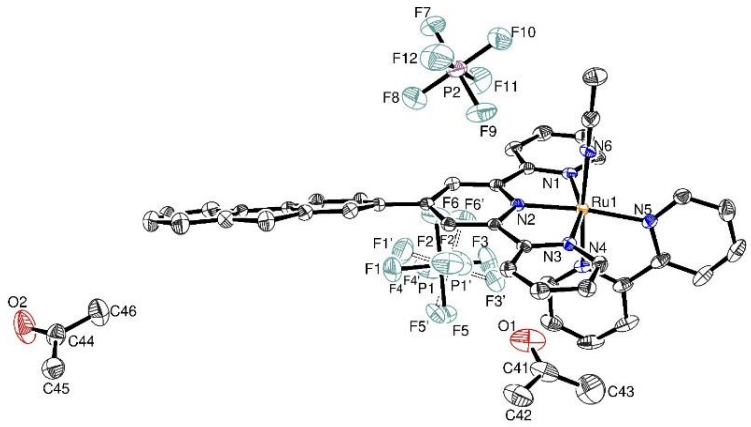

Figure 1 Asymmetric unit for [**RuMeCN-1**'](PF$_6$)$_2$. Formula $C_{40}H_{30}N_6Ru$, 2 PF_6, 2 C_3H_6O ; Formula weight 1101.87 ; Monoclinic ($P2_1/c$) ; *a* = 8.9330(13) Å, *b* = 19.725(3) Å, *c* = 26.047(4) Å, beta = 90.883(4) deg. T = 133(2) K ; Z = 4 ; R_1 [I>2sigma(I)] = 0.0463 ; wR_2 (all data) = 0.1023 ; GOF = 1.154.

*Synthesis of **[Ru(NO)Ru(MeCN)]-5***

As will be discussed below, the full understanding of the NO• release in **RuNO-5** will appear strongly related to the capability to determine precisely few key molecular parameters related to the anticipated intermediate **[Ru(NO)Ru(MeCN)]-5**, in which a single NO• is released. Achieving this goal rises the challenging issue of the chemical synthesis of this species. The targeted complex was successfully synthetized using a multi-step reaction sequence illustrated in Scheme **2**. This strategy involved the stepwise formation of the final asymmetric complex by independently synthesizing each component, the monometallic components **4** and **8**. The obtention of compound **1** followed the procedures outlined in previous reports, ensuring reproducibility and reliability.[16] The complexation route began by the metalation of iodinated terpyridine **1** using $RuCl_3 \cdot xH_2O$ (*i*), resulting in the formation of the neutral Ru^{III} complex **2** with high yields. In the subsequent step, two chlorido ligands were replaced by 2,2'-bipyridine, with the concomitant reduction of Ru^{III} to Ru^{II}, leading to the formation of complex **3** (*ii*). Then, an efficient ligand exchange reaction with MeCN under an argon atmosphere was employed. This was followed by a metathesis reaction with aqueous NH_4PF_6, resulting in the formation of complex **4**.

The synthesis of **[Ru(NO)Ru(MeCN)]-5** continued by the preparation of ligand **5**, which was conveniently synthesized from compound **1** through a Sonogashira cross-coupling reaction. In this synthetic pathway, the trimethyl silane moiety was intentionally retained until the preceding step, acting as a protecting group to prevent undesired oxidative side reactions arising from the interaction between the ruthenium salt and the terminal acetylene.[22] The complexation of ligand **5** followed a similar procedure as the previous reaction (*i*), leading to the formation of complex **6**. Subsequently, two chlorido ligands were replaced by 2,2'-bipyridine, as described in reaction (*ii*). In addition, K_2CO_3 was employed

to remove the trimethyl silane group, resulting in the successful synthesis of complex **7** with a satisfactory yield. The next step involved an efficient ligand exchange reaction with $NaNO_2$, followed by metathesis with aqueous NH_4PF_6, yielding complex **8**. Notably, both complexes **4** and **8** shared the same counteranion (PF_6^-) to prevent any potential solubility issues in subsequent reactions.

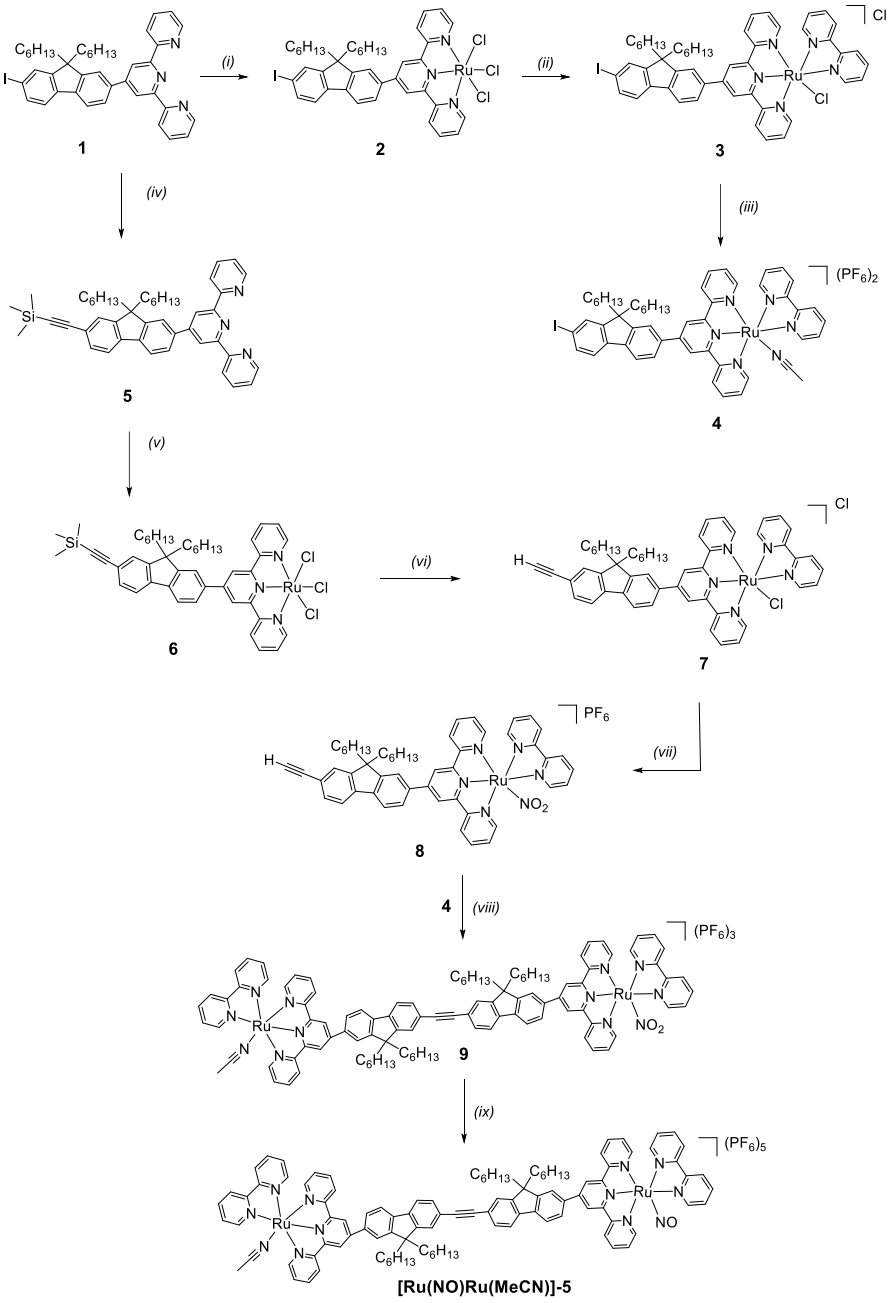

Scheme 2. Synthesis of **[Ru(NO)Ru(MeCN)]-5**. Reagents and conditions: (*i*,*v*) $RuCl_3 \cdot xH_2O$, EtOH, reflux (84–92 %) (*ii*) LiCl, Et_3N, EtOH/H_2O, reflux (58 %); (*iii*) MeCN/H_2O, Ar, reflux then NH_4PF_6(aq) (90 %); (*iv*) $Pd(PPh_3)_2Cl_2$, ethynyltrimethylsilane, CuI, THF (43 %); (*vi*) LiCl, Et_3N, EtOH/H_2O, K_2CO_3, reflux (64 %); (*vii*) $NaNO_2$, EtOH/H_2O, reflux then NH_4PF_6(aq) (92 %); (*viii*) $Pd(PPh_3)_2Cl_2$, CuI, THF/Et_3N, reflux (7 %); (*ix*) HCl, EtOH, 60°C, then NH_4PF_6(aq) (90 %).

To synthesize the C≡C coupled Ru^{II} complex **9**, we employed the versatile Sonogashira cross-coupling reaction.[23] This method serves as an excellent way for covalently linking two large molecules, offering several advantages for our synthetic goals. Notably, this approach operates under relatively mild reaction conditions. Additionally, it exhibits excellent compatibility with various functional groups, eliminating the risk of introducing unwanted reactive metal centers or substituents into our target complex.

After purification, the nonsymmetric complex **9** was treated with concentrated hydrochloric acid, followed by metathesis with aqueous NH_4PF_6 to yield the desired **[Ru(NO)Ru(MeCN)]-5** complex. The FTIR spectra of the final product exhibited characteristic ν(NO) vibrations of ν= 1933 cm^{-1}. Within this range, the electronic configuration of Ru-NO can be formally considered as diamagnetic Ru^{II}-NO^+.[24]

The completeness of the complex synthesis at each step was evaluated using ^{1}H-NMR analyses. Notable changes in chemical shift were observed for the hydrogen atoms in relative *ortho* position to the annular nitrogen of the equatorial rings of the bpy ligands (H-31, H-69). This is attributed to their spatial proximity to the varying monodentate ligands (X, Y).

The ^{1}H-NMR spectrum (Figure **2**) of **[Ru(MeCN)Ru(NO_2)]-5** (H-31 : δ = 9.94 and H-69 : δ = 10.04 ppm) can be regarded as a superposition of the spectra obtained for the symmetric molecules **[Ru(NO_2)Ru(NO_2)]-5** (H-69 : δ = 10.06 ppm) and **[Ru(MeCN)Ru(MeCN)]-5** (H-31: δ = 9.96 ppm). Consequently, nearly identical chemical shift values were observed for all hydrogens and carbons between the symmetrical complexes and the nonsymmetrical one. This observation indicates that the two sides of the **[Ru(MeCN)Ru(NO_2)]-5** complex exhibit independent behavior. Thus, alterations in one extremity of the complex do not influence the other extremity, highlighting the distinct and autonomous nature of each side. For a comprehensive characterization, please refer to the *Supporting Information* (Tables **1, 4, 5**).

A similar behavior was observed in the final complex **[Ru(MeCN)Ru(NO)]-5**. *Supporting Information* contains the corresponding Figure with all the data required for a comprehensive analysis of the complex, including detailed spectroscopic data, (Tables **2** and **6)**.

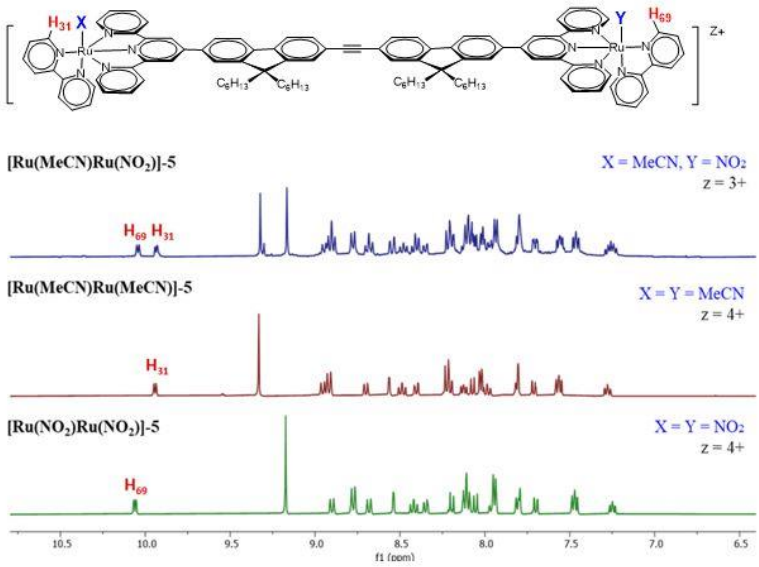

Figure 2. Aromatic region of the ^{1}H-NMR spectrum for (top) **[Ru(MeCN)Ru(NO$_2$)]-5**, (z = 3+), ((CD$_3$)$_2$CO, 600 MHz), (middle) **[Ru(MeCN)Ru(MeCN)]-5**, (X = Y, H$_{31}$ = H$_{69}$, z = 4+), (bottom) **[Ru(NO$_2$)Ru(NO$_2$)]-5**, (X = Y, H$_{31}$ = H$_{69}$, z = 2+).

2.2. UV-visible spectroscopy

The UV-visible spectra of five **RuMeCN-1,5** compounds synthetized chemically (route *b* in Scheme 1) are gathered in Figure 3. Importantly, they can be superimposed with the photoproducts obtained from the irradiation of the five **RuNO-1** to **RuNO-5** complexes at various wavelengths (route *a* in Scheme 1). This is exemplified for **RuMeCN-5** in Figure 4 (comparisons are provided in *Supporting Information* for **RuMeCN-1** to **RuMeCN-4**). Previous EPR experiments show that NO$^{\bullet}$ is generated during the irradiation process. It is then trapped by an iron complex and detected by the appearance of a triplet signal easily identified as the signature of NO$^{\bullet}$, resulting from the hyperfine coupling between the radical and the spin of the nitrogen atom (I=1).[16,21,25] Therefore, the photoproducts are all identified as **RuMeCN-1,5**, corresponding to the complexes in which the nitrosyl ligands are fully replaced by molecules of solvents (acetonitrile). Although the final photoproducts are not isolated after irradiation (route *a*), the identification of the complexes with those obtained by route *b* allows us to determine unambiguously the key parameters (absorption maxima λ_{max} and absorption coefficients ε) for **RuMeCN-1** to **RuMeCN-5**. Table 1 gathers ε values measured at selected wavelengths, which will be used in the two-step model developed in section **2.3.** to fully characterize the release processes.

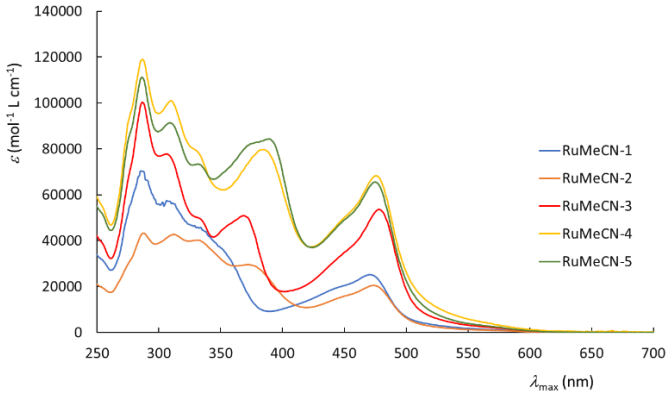

Figure 3. UV-visible spectra in MeCN for the **RuMeCN-1,5** series.

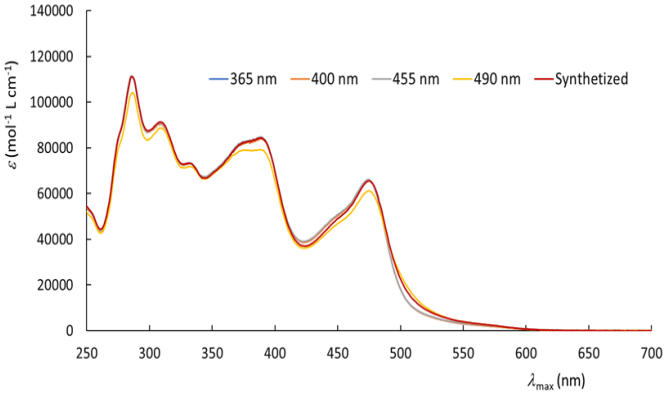

Figure 4. UV-visible spectra of **RuMeCN-5** in MeCN obtained by irradiation at various wavelengths or chemically synthetized, respectively routes *a* and *b*, described in Scheme 1.

Table 1 Extinction coefficient (ε in mol^{-1} L cm^{-1}) at the absorption maxima (λ_{max} in nm) and at selected wavelengths for the five **RuMeCN-1,5** complexes and **[Ru(NO)Ru(MeCN)]-5**, isolated after chemical synthesis (Scheme 1b).

		selected wavelengths of irradiation			
compound	ε (λ_{max})	365 nm	400 nm	455 nm	490 nm
RuMeCN-1	25 120(470)	24 070	10 180	21 250	12 130
RuMeCN-2	20 550(474)	29 150	15 990	16 610	11 900
RuMeCN-3	53 590(478)	50 060	17 810	37 050	37 530
RuMeCN-4	68 330(476)	68 210	62 120	52 690	44 790
RuMeCN-5	65 650(475)	77 460	69 640	51 360	40 550
[Ru(NO)Ru(MeCN)]-5	49 370(472)	67 790	46 780	43 390	38 680

Having isolated the intermediate **[Ru(NO)Ru(MeCN)]-5** complex provides a unique opportunity to extract its ε value, which will appear to be of prime importance to determine the mechanism of the

photoreaction from **RuNO-5** to **RuMeCN-5** (*Vide Infra*). The three spectra available along the **5** series ([Ru(NO)Ru(NO)] → [Ru(NO)Ru(MeCN)] → [Ru(MeCN)Ru(MeCN)]) are presented in Figure 5. Interestingly, the spectrum of the intermediate appears to be grossly the average between that of the starting RuNO complex and that of the photoproduct.

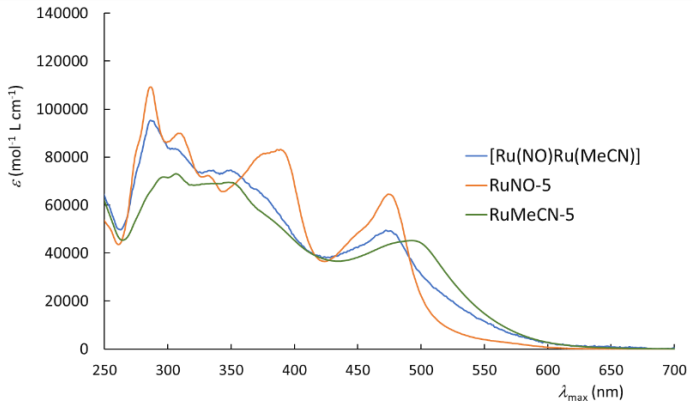

Figure 5. UV-visible spectra of **RuNO-5**, **RuMeCN-5**, and the intermediate [**Ru(NO)Ru(MeCN)]-5** complex in MeCN.

2.3. Spectrokinetic studies for the bimetallic complexes

The purpose of the present contribution is to provide a full understanding of the NO• release in bimetallic species, either through a one-step (equation 2) or a two-step (equation 3) process. A one-set process could reproduce the experimental data in two situations (*i*) the release of two NO• after a single electronic transition, or (*ii*) the extremely fast reactivity of the intermediate Ru(NO)Ru(MeCN) species (quasi stationary state approximation), two explanations which hardly fit with the chemical intuition. Indeed (*i*) although the [RuNO] fragments are related by symmetry in the bimetallic species, they are never chemically equivalent at a given time in a given complex. This implies that they are not subjected to the same charge transfer effect during the electronic transition, therefore they do not exhibit the same capability to lead to NO• release. Similarly, (*ii*) the UV-visible spectrum of the intermediate Ru(NO)Ru(MeCN) complex compared with those of the initial RuNO and final RuMeCN complexes does not reveal any specificity which would lead to strongly enhanced photoreactivity, after the release of the first NO•.

In an attempt to clarify the photochemical properties of these bimetallic complexes, experiments were carried out at four different irradiation wavelengths (λ = 365, 400, 455 and 490 nm) to increase the number of experimental data, thus providing a better accuracy in the fitting procedures.[26]

Both one-step ($A \rightarrow C$) and two-step model ($A \rightarrow B \rightarrow C$) were envisioned to analyze the effect of the irradiation. The experimental basis of the kinetic study consists of the spectral evolutions recorded under continuous irradiation. The initial spectra (t=0) are recorded just before irradiation and correspond to the bimetallic **RuNO-3,4,5** complexes. In each case, the recordings are made until the absorbance no longer varies, indicating total transformation of the reactant into the final photoproduct. As pointed out before, the final spectra correspond to the complexes **RuMeCN-3,4,5** identical to the species obtained by chemical synthesis. The photorelease experiments are exemplified in Figure 6 for the three **RuNO-3,4,5** complexes under irradiation at 365 nm (**RuNO-3** and **RuNO-5**) and at 400 nm (**RuNO-4**), where the evolution of the absorbance at the crossover points are particularly visible.

The presence of up and down arrows in Figure 6a indicates reversals of direction over time, which implies the appearance of crossover points between the spectra, which correspond to wavelengths where the absorption stays relatively constant all over the photoreaction. The careful examination of the evolution of the absorbance over time provides the key to determine the mechanism, either in one or two steps (Figure 6b). If all crossover points between the initial and final spectra give rise to a perfectly horizontal evolution, they are said to be isosbestic and indicate the direct transformation of the reactant into the product ($A \rightarrow C$). On the other hand, if only one of these points deviates from the horizontal, this indicates that a third compound is involved during the photoreaction ($A \rightarrow B \rightarrow C$). The experimental data for **RuNO-3,4,5** can be described as follows:

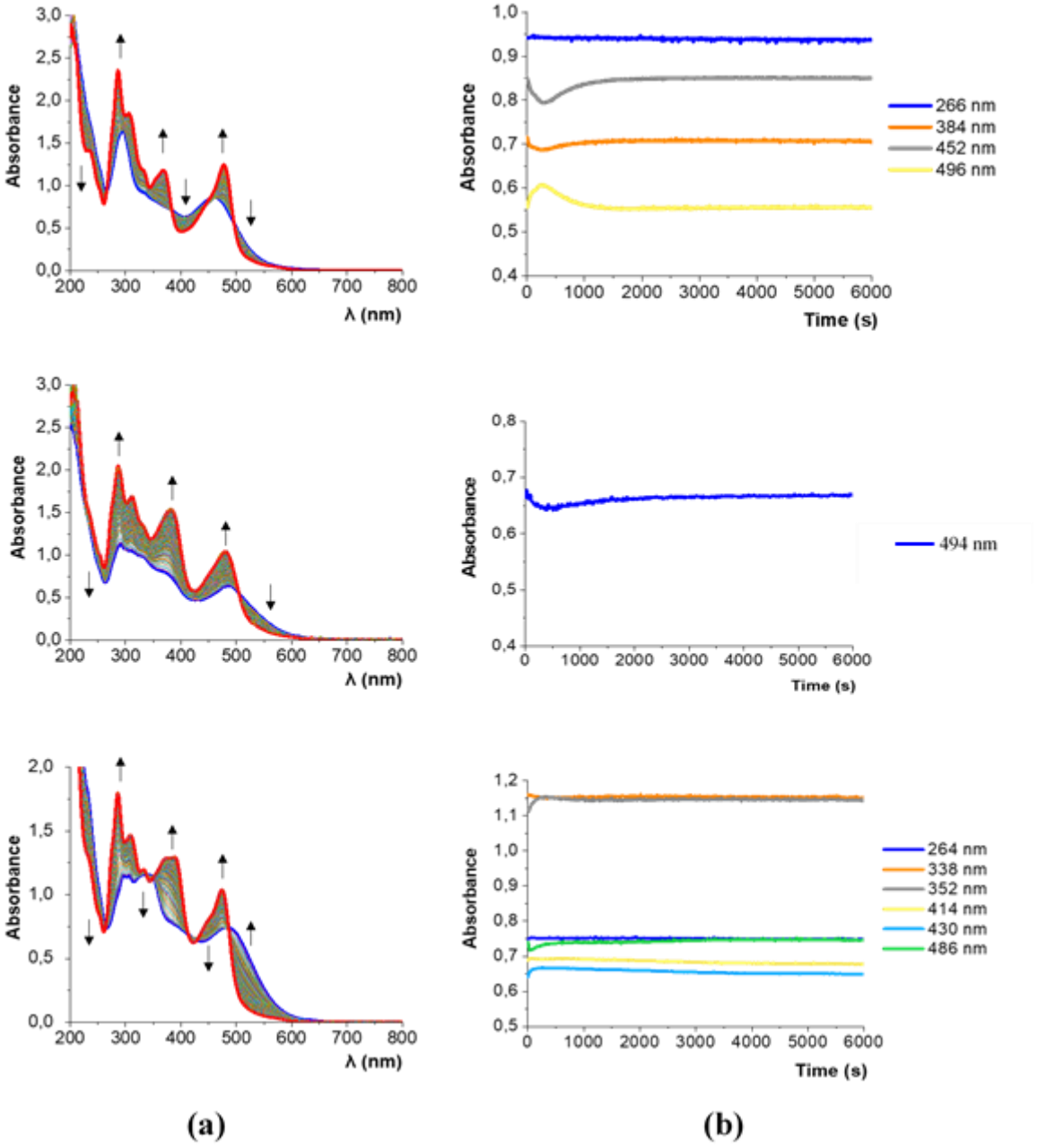

Figure 6 (a) Spectral evolution under irradiation at 365 nm, for **RuNO-3** (top) and **RuNO-5** (bottom), at 400 nm for **RuNO-4** (middle). The arrows indicate the direction of absorbance evolution. (b) Kinetics recorded at the crossover points.

RuNO-3: For the experiment under irradiation at 365 nm, the crossover points are observed at 266, 384, 452 and 496 nm. The kinetic records at these crossover points (top of Figure 6b) shows that the absorbance at 266 nm remains perfectly invariant during irradiation. Nevertheless, variations appear at other wavelengths, which undoubtedly indicate the presence of a reaction intermediate: a first photochemical step yields **[Ru(NO)Ru(MeCN)]-3**, which then reacts to release the second NO• molecule. The shape of the kinetics provides information on the relative values of the absorption

coefficients (ε) for the three *A*, *B*, *C* compounds: (*i*) at 266 nm the spectra of the three compounds show a point of intersection. Therefore they possess nearly identical ε ($\varepsilon_A \approx \varepsilon_B \approx \varepsilon_C$) ; (*ii*) at 384 and 452 nm, the absorbance initially decreases, then increases which leads to $\varepsilon_B < \varepsilon_A \approx \varepsilon_C$; the opposite situation is observed at 496 nm with an initial increase of absorbance, therefore $\varepsilon_B > \varepsilon_A \approx \varepsilon_C$. Although the **[Ru(NO)Ru(MeCN)]-3** intermediate could not be synthesized, its presence during irradiation is clearly visible. The reaction proceeds in two successive photochemical steps.

RuNO-4: Only one crossover point is observed at 494 nm for the experiments irradiated at 365, 400 and 455 nm, while it appears at 488 nm for the irradiation at 490 nm. The shape of the kinetics (here recorded for the irradiation at 400 nm) shows a low amplitude deviation with an initial decrease of the absorbance followed by a slow increase indicating the presence of an intermediate with $\varepsilon_B < \varepsilon_A \approx \varepsilon_C$. Such small deviation of the kinetic curves only observed around the intersection point could appear as a poor confirmation of the presence of the intermediate but a second feature confirms its presence in the kinetic curves obtained at the three irradiation wavelengths (see Figure 8) as after a rapid increase at the beginning, the absorbance continues to slowly increase on a much longer duration than for **RuNO-3**. Such a dynamics cannot be reproduced by a simple $A \rightarrow C$ process.

RuNO-5: The crossover points of the reactant and final product spectra are obtained at λ = 264, 338, 352, 414, 430 and 486 nm. The kinetics at these wavelengths (bottom of Figure 6b) show that the absorbance at 264, 338 and 414 nm is virtually horizontal, whereas 352, 430 and 486 nm show low amplitude deviations accounting for the presence of an intermediate. Kinetic curves recorded at the four irradiation wavelengths (see Figure 9) show in all cases monotonic increase or decrease. This is in line with the relative position of the spectra of the three compounds at these wavelengths, for which the absorption coefficients always vary in the order A, B, C with increasing or decreasing values.

2.4. Kinetic modelling

The model must be able to reproduce a large experimental base while ensuring the consistency of the parameters. The data set to be reproduced consists of the four experiments (3 for **RuNO-4**) performed at the four irradiation wavelengths (3 for **RuNO-4**), for each of which the kinetics at these four wavelengths are to be reproduced (16 curves/12 curves). The differences in behavior noted in the spectral studies and in the form of the kinetic curves to be reproduced will enable us to demonstrate the value of kinetic modeling in two situations. For **RuNO-3** and **RuNO-4**, the presence of an intermediate having been unambiguously demonstrated, the reaction mechanism can be represented by equations 3a and 3b ($A \rightarrow B \rightarrow C$).[27] Then, understanding the complete photorelease process leads to determine the

spectrum of the intermediate *B* and the two quantum yields (ϕ_{AB}^{λ} and ϕ_{BC}^{λ}) defined as the number of mole of NO$^{\bullet}$ released per mole of photons absorbed by *A* and *B*, respectively, as illustrated below:

$$A \xrightarrow{\phi_{AB}^{\lambda}} B \xrightarrow{\phi_{BC}^{\lambda}} C \qquad (4)$$

In the case of **RuNO-5**, the formation of the intermediate does not clearly appear on the experimental set. We will need first to rule out the possibility to reproduce the curves with a direct transformation of *A* into *C*. When the possibility to reproduce the kinetic curves with a one step process is discarded we will show that the kinetics recorded are compatible with the results obtained independently on the synthetized intermediate compound **[Ru(NO)Ru(MeCN)]-5**.

The rate of the photochemical processes r_i, where *i* represents the photoreactive reactant (*A* or *B*) is expressed as follows:

$$r_i = -\phi_{ij}^{\lambda}\, \varepsilon_i^{\lambda}[i]\, l_r\, I_0^{\lambda} F^{\lambda} \qquad (5)$$

In this equation, F^{λ} is the photokinetic factor, l_r is the photochemical reactor irradiation optical path, ϕ_{ij}^{λ} is the quantum yield of the photochemical reaction of *i* transformed in *j* (*B* when *i* = *A*, or *C* when *i* = *B*) at the irradiation wavelength λ, I_0^{λ} is the intensity of the irradiation photon flux at λ. The photokinetic factor F^{λ} is expressed as $F^{\lambda} = (1 - 10^{-Abs^{\lambda}})/Abs^{\lambda}$, in which Abs^{λ} is the total absorbance of the absorbing species at the irradiation wavelength λ ($Abs^{\lambda} = (\varepsilon_A^{\lambda}[A] + \varepsilon_B^{\lambda}[B] + \varepsilon_C^{\lambda}[C])\, l_r$).

The differential equations giving the evolution of A, B and C are given by:

$$\frac{d[A]}{dt} = -r_A \quad ; \quad \frac{d[B]}{dt} = r_A - r_B \quad ; \quad \frac{d[C]}{dt} = r_B \qquad (6a\text{-}c)$$

In the framework of the present model, we consider that quantum yields depend on irradiation wavelengths, so each experiment is independent for these parameters. For multi-experiment fitting to be of interest, the experiments must be coupled by a parameter common to all four experiments (three for **RuNO-4**). This is the spectrum of compound *B*, which ensures consistency of results across the different experiments. The results as presented as follows:

RuNO-3: The parameters to be determined are the two quantum yields (ϕ_{AB}^{λ} and ϕ_{BC}^{λ}) at the four irradiation wavelengths (λ) and the spectrum of the intermediate, in order to extract ε_B^{λ} at the different wavelengths. The kinetic evolution under irradiation at 365, 400, 455, and 490 nm are shown in Figure

7 for **RuNO-3**. For each wavelength, the measurements are performed at the four different wavelengths, including the irradiation wavelength. Therefore, and for a better consistency within the four irradiation experiments, the wavelengths of measurements are also 365, 400, 455, and 490 nm.

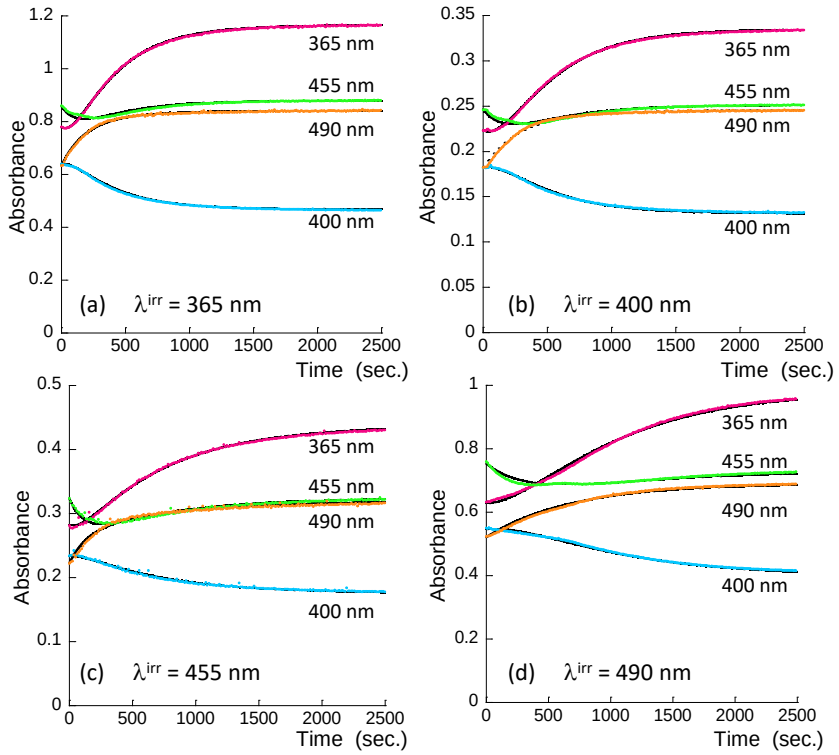

Figure 7 Kinetic evolution under continuous irradiation at a) λ^{irr} = 365 nm ; b) λ^{irr} = 400 nm ; c) λ^{irr} = 455 nm ; d) λ^{irr} = 490 nm for **RuNO-3**. Coloured symbols are the experimental points at the four wavelengths; continuous black lines are given by the model.

The experimental curves are perfectly reproduced by the model. The parameters obtained are listed in Table 2. The values are consistent with previous observations as the quantum yields decrease with increasing irradiation wavelength for both the reactant and intermediate. The standard deviation values obtained for ε_B (about 3 %) to get the best fit remain within the order of magnitude of the experimental ones for ε_A and ε_C.

Table 2 Quantum yields ϕ_{AB}^{λ} and ϕ_{BC}^{λ} and ε_B^{λ} obtained by modelling for **RuNO-3**. The standard deviations are obtained by the parameter $\Delta\varepsilon^{\lambda}$ in the model (see *Experimental Section*). Absorption coefficients ε_A and ε_C were obtained experimentally.

λ (nm)	$\phi_{AB}^{\lambda} \pm 0.001$	$\phi_{BC}^{\lambda} \pm 0.001$	$\varepsilon_A^{\lambda} \pm \Delta\varepsilon_A^{\lambda}$ (L.mol^{-1}.cm^{-1})	$\varepsilon_B^{\lambda} \pm \Delta\varepsilon_B^{\lambda}$ (L.mol^{-1}.cm^{-1})	$\varepsilon_C^{\lambda} \pm \Delta\varepsilon_C^{\lambda}$ (L.mol^{-1}.cm^{-1})

365 nm	2.9×10^{-2}	1.8×10^{-2}	32400 ± 990	31300 ± 200	49500 ± 800
400 nm	1.9×10^{-2}	0.7×10^{-2}	27000 ± 300	28600 ± 600	37030 ± 300
455 nm	1.9×10^{-2}	0.4×10^{-2}	36900 ± 300	31000± 1000	37030 ± 600
490 nm	0.6×10^{-2}	0.5×10^{-2}	26300 ± 900	32800 ± 1100	35900 ± 800

The model delivers the concentrations of *A*, *B* and *C* at all times, allowing the determination of the spectrum of *B* at all wavelengths (*Supporting Information*, Figures **113**). It is interesting to point out that the low amplitude relative variations of ε_A, ε_B and ε_C at the crossover points described in section 2.3 (Figure 6) are all correctly predicted although this wavelength was not chosen for the fitting procedure. The isosbestic point observed at 266 nm corresponds exactly to an intersection point of the three spectra. The concentration of NO$^{\bullet}$, given by $[NO^{\bullet}] = [A]_0 - [A] + [C]$ (*Supporting Information*, Figures **114**) is also obtained. The proportion of *B* formed during the reaction is high in each case in relation with the general observation that $\phi_{AB}^{\lambda} > \phi_{BC}^{\lambda}$. The maximum concentration of *B* relative to the initial concentration of *A* increases for the first three irradiation wavelengths, rising steadily from 46% at 365 nm to 64% at 455 nm, then dropping to 37% at 490 nm, where ϕ_{AB}^{λ} is only slightly larger than ϕ_{BC}^{λ}. The concentration of NO$^{\bullet}$ produced by the reaction increases rapidly at first, and then continues during the formation of *C*.

RuNO-4: As for **RuNO-3**, the parameters to be determined are the two quantum yields (ϕ_{AB}^{λ} and ϕ_{BC}^{λ}) and the spectrum of the intermediate. For this compound we could only use the three experiments recorded under irradiation at 365, 400 and 455 nm. Indeed, as mentioned before, the crossover point observed at 494 nm for these three experiments is displaced to 488 nm for the irradiation at 490 nm. At that point, we do not know the origin of such discrepancy but it clearly appeared that coherent parameters could not be extracted by including this experiment in our set. The origin of this difference is beyond the scope of this study, we have hence only analyzed the experiments performed with the three first irradiation wavelengths. The kinetic evolution under irradiation at 365, 400 and 455 nm are shown in Figure 8 for **RuNO-4**.

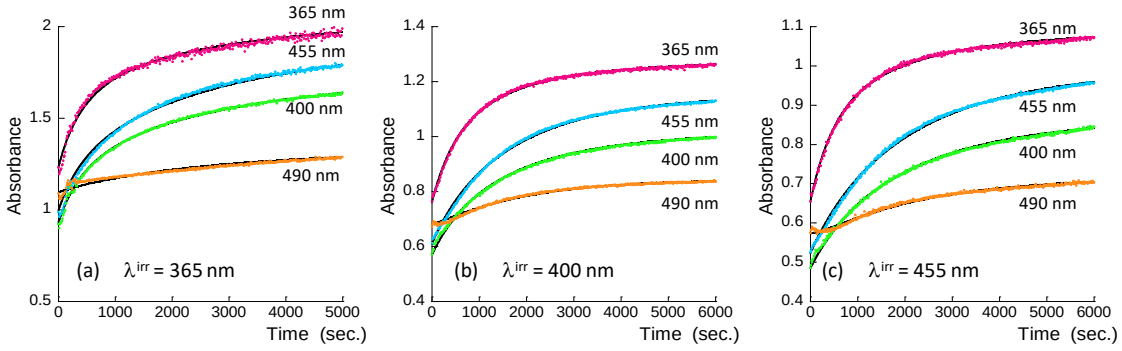

Figure 8 Kinetic evolution under continuous irradiation at a) λ^{irr} = 365 nm ; b) λ^{irr} = 400 nm ; c) λ^{irr} = 455 nm for **RuNO-4**. Coloured symbols are the experimental points at the three wavelengths; continuous black lines are given by the $A \rightarrow B \rightarrow C$ model.

The experimental curves are adequately reproduced by the two-step model. The parameters obtained are listed in Table 3. As for **RuNO-3**, the quantum yields decrease with increasing irradiation wavelength for both the reactant and intermediate and $\phi_{AB}^{\lambda} > \phi_{BC}^{\lambda}$. The standard deviation values obtained for ε_B (about 7 %) to get the best fit remain within the order of magnitude of the experimental ones for ε_C.

Table 3 Quantum yields ϕ_{AB}^{λ} and ϕ_{BC}^{λ} and ε_B^{λ} obtained by modelling for **RuNO-4**. The standard deviations are obtained by the parameter $\Delta\varepsilon^{\lambda}$ in the model (see *Experimental Section*). Absorption coefficients ε_A and ε_C were obtained experimentally.

λ (nm)	$\phi_{AB}^{\lambda} \pm 0.001$	$\phi_{BC}^{\lambda} \pm 0.001$	$\varepsilon_A^{\lambda} \pm \Delta\varepsilon_A^{\lambda}$ (L.mol^{-1}.cm^{-1})	$\varepsilon_B^{\lambda} \pm \Delta\varepsilon_B^{\lambda}$ (L.mol^{-1}.cm^{-1})	$\varepsilon_C^{\lambda} \pm \Delta\varepsilon_C^{\lambda}$ (L.mol^{-1}.cm^{-1})
365 nm	1.5×10^{-2}	0.2×10^{-2}	40620 ± 300	57560 ± 2000	67350 ± 800
400 nm	0.8×10^{-2}	0.2×10^{-2}	32550 ± 200	42840 ± 2000	6200 ± 300
455 nm	0.6×10^{-2}	0.1×10^{-2}	30660 ± 400	40100± 2600	55000 ± 1600

All the quantum yields obtained for **RuNO-4** are lower than the ones obtained for **RuNO-3** in line with a longer duration of the photoreaction. The proportion of *B* formed during the reaction is again high (*Supporting Information*, Figure **116**). The maximum concentration of *B* relative to the initial concentration of *A* are in all cases around 60% for the three irradiation wavelengths (67, 61 and 63% for respectively irradiation at 365, 400 and 455 nm). The concentration of NO• produced by the reaction follows the same trend as for **RuNO-3**, it rapidly increases at first, and then continues during the slow formation of *C*. However, in this case the slow release of NO last about three times longer due to the lower global reactivity of this compound.

RuNO-5: As mentioned above, the presence of the reaction intermediate is hardly visible in the shape of the recorded kinetics, which all show a monotonic evolution. As a first step, it is therefore advisable to check that these curves cannot be reproduced by a direct transformation of the reactant into the product. In the case of a mechanism that can be represented by the following reaction:

$$A \xrightarrow{\phi_{AC}^{\lambda}} C \qquad (8)$$

Within this simplified scheme, the only adjustable parameter is $\phi_{AC}{}^{\lambda}$, the values of ε_A and ε_C being fixed by the experimental data. Here, the four experiments, at the 365, 400, 455, and 490 nm irradiation wavelengths, are independent, but the model must reproduce the absorbance at all four wavelengths for the same value of $\phi_{AC}{}^{\lambda}$. The kinetic evolutions are shown in Figure 9. The best fit obtained by this model is represented by the dotted lines in figure. Note that the kinetics at 455 and 490 nm are perfectly reproduced, but the kinetics at 365 and 400 nm all deviate significantly from the experimental points. The model is therefore challenged by the multi-wavelength analysis. To reproduce the curves, the formation of the intermediate must be taken into account.

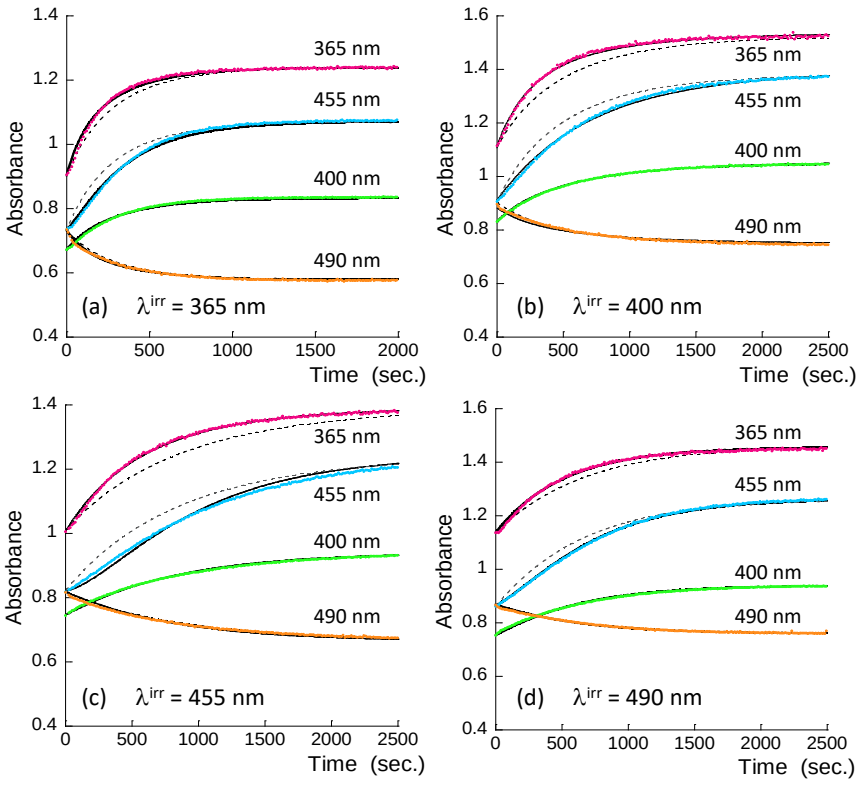

Figure 9 Kinetic evolution under continuous irradiation at a) λ^{irr} = 365 nm ; b) λ^{irr} = 400 nm ; c) λ^{irr} = 455 nm ; d) λ^{irr} = 490 nm for **RuNO-5**. Coloured symbols are the experimental points at the four wavelengths; dotted black lines correspond to the $A \rightarrow C$ model; continuous black lines are given by the $A \rightarrow B \rightarrow C$ model.

A fitting procedure similar to that applied to **RuNO-3**, which would deliver all three parameters, ϕ_{AB}^{λ}, ϕ_{BC}^{λ} and ε_B is not possible here, as the information provided by the kinetic curves is insufficient. Tests carried out in this direction led to inconsistent solutions with ε_B values being far removed from experimental values. Fortunately, the intermediate **[Ru(NO)Ru(MeCN)]-5** complex is available and perfectly characterized, thus providing the missing ϕ_{BC}^{λ} and ε_B parameters. Therefore, the only missing parameter is ϕ_{AB}^{λ}. After setting ϕ_{BC}^{λ} and ε_B to the values obtained previously *(Supporting Information*: Figure **111** and **112** and Table **15**), a perfect fit is obtained at all wavelengths and for all four experiments (black solid line in Figure 9). Note that the quality of the fit is such that the black lines are almost indistinguishable with the coloured lines in the Figure. The standard deviation values obtained for ε_B (less than 7 %) remain acceptable. Being able to reproduce with that precision the whole set of curves with such a low degree of liberty, (only two parameters fitted: ϕ_{AB}^{λ} and $\Delta\varepsilon_B$), is a strong indication of the validity of the two-step process and the extracted parameters. The parameters are listed in Table 4.

Table 4 Quantum yields ϕ_{AB}^{λ} obtained by the $A \rightarrow B \rightarrow C$ modelling for **RuNO-5**. Quantum yield ϕ_{BC}^{λ} obtained separately by the $B \rightarrow C$ modelling for **[Ru(NO)Ru(MeCN)]-5**. ε_A^{λ}, ε_B^{λ}, ε_C^{λ} and related standard deviations are experimental. For ε_B, the values reported are the mean values obtained for $\varepsilon_B^{\lambda} + \Delta\varepsilon_B^{\lambda}$ by the model (only $\Delta\varepsilon_B^{\lambda}$ is fitted), standard deviations reflect the variability given by the model for best fit.

λ (nm)	$\phi_{AB}^{\lambda} \pm 0.001$	$\phi_{BC}^{\lambda} \pm 0.001$	$\varepsilon_A^{\lambda} \pm \Delta\varepsilon_A^{\lambda}$ (L.mol^{-1}.cm^{-1})	$\varepsilon_B^{\lambda} \pm \Delta\varepsilon_B^{\lambda}$ (L.mol^{-1}.cm^{-1})	$\varepsilon_C^{\lambda} \pm \Delta\varepsilon_C^{\lambda}$ (L.mol^{-1}.cm^{-1})
365 nm	2.8×10^{-2}	0.9×10^{-2}	56800 ± 1100	69 300 ± 1500	76800 ± 600
400 nm	2.2×10^{-2}	0.8×10^{-2}	45400 ± 400	50000 ± 3400	67800 ± 2000
455 nm	0.9×10^{-2}	0.5×10^{-2}	41050 ± 1000	45500 ± 2400	51500 ± 1400
490 nm	0.8×10^{-2}	0.5×10^{-2}	45500 ± 300	41400 ± 2800	37500 ± 1000

As for **RuNO-3** and **RuNO-4**, the quantum yields decrease with increasing irradiation wavelength for both the reactant and intermediate and $\phi_{AB}^{\lambda} > \phi_{BC}^{\lambda}$. The concentrations of *A*, *B* and *C* calculated by the model also show a significant accumulation of *B* in the reaction medium for **RuNO-5**, around 60% for irradiations at 365 and 400 nm and around 50% at 455 and 490 nm. NO$^{\bullet}$ production kinetics are qualitatively similar to those observed for **RuNO-3**, and **RuNO-4**.

A comparison between the three bimetallic compounds show a higher photoreactivity for **RuNO-3** and **RuNO-5** for both the reactant and the intermediate than for **RuNO-4**. $\phi_{AB} > \phi_{BC}$ is systematically observed for the three complexes at any wavelengths. Although the dispersion in the ϕ_{AB} / ϕ_{BC} ratio is very large, with values ranging from 1.2 (**RuNO-3** at 490 nm) to 7.5 (**RuNO-4** at 365 nm), the averaged

value is around 2.5. This might somewhat illustrate the fact that two nitrosyls are available in the starting complexes and only one in the intermediate.

In comparison, the monometallic species exhibit the following quantum yield. **RuNO-1**: $\phi = 0.8\times10^{-2}$, 0.6×10^{-2} and 0.2×10^{-2} for irradiation at 365, 400, and 455 nm, respectively. **RuNO-2**: $\phi = 1.2\times10^{-2}$, 0.8×10^{-2} and 0.7×10^{-2} for irradiation at 365, 400, and 455 nm, respectively. (*Supporting Information*, Table **11** and **12**). While these quantum yield values lie in the same range of magnitude than those of the bimetallic species at the ϕ_{BC} step, they are lower than those observed for ϕ_{AB}. This allows establishing the relevance of the bimetallic approach at both quantum yield (ϕ) and TPA (σ_{TPA}) level, taking into account the fact that the overall efficiency of the NO delivery achieved under two-photon irradiation is the encaging parameter defined as the $\phi \times \sigma_{TPA}$) product.[25a,27]

3. CONCLUSION

RuNO-3, **RuNO-4** and **RuNO-5** are bimetallic RuNO complexes, which exhibit NO• photorelease capabilities under a large range of irradiation wavelengths. The chemical synthesis of the photoproducts, in which the nitrosyls are replaced by acetonitrile, and moreover that of the intermediate **[Ru(NO)Ru(MeCN)]**, allow to fully elucidate the kinetics of the photorelease processes using a model in two steps specially designed for the purpose of this investigation. In the case of **RuNO-3** and **RuNO-4**, multi-experiments modelling enabled us to determine quantum yields at all irradiation wavelengths and the *B* spectrum using unambiguous experimental data. In the case of **RuNO-5**, the spectral properties of the compounds involved are particularly unfavorable, but the model has enabled us to definitively rule out the possibility of a one-step process and to demonstrate the compatibility of the experimental data recorded for the intermediate obtained by the synthetic path with the two-step process and related parameters. Moreover, the quantum yield of NO• release investigated in these three cases makes these exogenous NO• donors particularly appealing for potential therapeutic applications.

4. EXPERIMENTAL SECTION

A homemade program SA, available in ref. 28, was used to model the reaction and fit the kinetic data. The first stage of the calculation involves numerical integration (semi-implicit Runge-Kutta method) of the differential equations defined by equations (5) and (6a-c). The calculation is performed for the four experiments (three for **RuNO-4**) recorded under irradiation at 365, 400, 455 and 490 nm (490 nm is missing for **RuNO-4**). The evolution of the concentrations thus obtained, the temporal variations in Absorbance can be calculated at the chosen wavelengths. For each experiment, the experimental base to be reproduced is made up of four wavelengths which, in order to have a common experimental base for

all experiments, are also the irradiation wavelengths. In fact, the irradiation wavelength must imperatively be part of the experimental base, as it determines the variation in the photokinetic factor F^{λ} and therefore the calculation of concentrations. For each experiment, we hence have data at the irradiation wavelength and three observation wavelengths distributed across the spectral range. The experimental base is thus made up of the four experiments (three for **RuNO-4**) monitored at 4 wavelengths, *i.e.* 16 experimental curves (12 for **RuNO-4**). The model parameters are: the intensity of the irradiation photon flux at λ, I_0^{λ} (mol.L^{-1}.s^{-1}), the quantum yields (ϕ_{AB}^{λ} and ϕ_{BC}^{λ}) which are assumed to depend on the irradiation wavelength, the optical path l_r (= 1 cm) and the absorption coefficients ε_i^{λ} at the four irradiation wavelengths. While the first two parameters are specific to each experiment, the values of ε_i^{λ} are common to all four experiments (three for **RuNO-4**). It is this parameter that ensures the consistency of the model results based on the four experiments (three for Ru-NO4), which is essential for their validation.

I_0^{λ} (mol.L^{-1}.s^{-1}) was obtained by measuring the power of the light intensity (5-6 mW) with a power meter from Thorlabs considering a volume of 2.5 mL, ε_A^{λ} and ε_C^{λ} are given by the initial (t = 0 just before irradiation is set on) and final ($t \rightarrow \infty$, Abs^{λ} is constant with time) spectrum. To take into account the variability in the experimental values of ε_A^{λ} and ε_c^{λ} from one experiment to another (see table 1 and 2), ε_j^{λ} is replaced in the model by ($\varepsilon_j^{\lambda} + \Delta\varepsilon_j^{\lambda}$). The values of $\Delta\varepsilon_j^{\lambda}$ are set by the experimental data for *A* and *C* for each experiment and for each wavelength. For the quantum yield value ϕ_{AB}^{λ} (given by the initial slope of the kinetics) to be correctly evaluated by the model, it is essential that the value of $A^{\lambda}(t=0)$ is perfectly reproduced. For the reaction product, this modulation makes it possible to reproduce the photostationary state without any adjustment to ε_C^{λ}. For *B*, ε_B^{λ} and $\Delta\varepsilon_B^{\lambda}$ were fitted for **RuNO-3** and **RuNO-4**. In the case of **RuNO-5** only $\Delta\varepsilon_B^{\lambda}$ was fitted. The experimental error given in table 1 and 2 represent $\Delta\varepsilon_j^{\lambda}$. The uncertainty in the quantum yield values is evaluated during the adjustment procedure. For the first calculation, only quantum yields and ε_B^{λ} values are optimized. In a second step, these parameters are fixed and the values of $\Delta\varepsilon_B^{\lambda}$ optimized. All parameters are then released to obtain the best fit of the data. In this final step, the quantum yield values initially obtained are varied to the fourth decimal place, enabling the error in quantum yield determination to be assessed at ± 0.001. The unknown parameters were fitted automatically using an iterative algorithm of the Powell type, designed to minimize the residual quadratic error $E = \Sigma j\, \Sigma i\, [cij - eij]2/(n \cdot N)$ where *cij* and *eij* are the computed and experimental values respectively, *n* is the number of data point in a given run, and *N* is the number of runs.

ACKNOWLEDGMENTS

P. L.-V. acknowledges support from the French National Research Agency under program ANR-18-CE29-0012.

ASSOCIATED CONTENT

Supporting information

Experimental procedures, NMR and Mass Spectrometry for products and intermediates, X-ray data for for [**RuMeCN-1'**]$(PF_6)_2$ (CCDC 2310622), NO˙ release data and kinetics, UV-visible spectroscopy (147 pages).

AUTHOR INFORMATION

Corresponding Authors

Pascal G. Lacroix – *Laboratoire de Chimie de Coordination du CNRS, 205 route de Narbonne, F-31077 Toulouse, France.*

Email : pascal.lacroix@lcc-toulouse.fr

ORCID : 0000-0002-5676-6924

Véronique Pimienta – *Laboratoire SOFTMAT,* Université Toulouse III, 118 Rte de Narbonne, 31062 Toulouse.

Email : veronique.pimienta@univ-tlse3.fr.

ORCID : 0000-0001-5134-5293

Isabelle Malfant – *Laboratoire de Chimie de Coordination du CNRS, 205 route de Narbonne, F-31077 Toulouse, France.*

Email : isabelle.malfant@lcc-toulouse.fr

ORCID : 0000-0002-1185-2124

Authors

Yael Juarez-Martinez – *Laboratoire de Chimie de Coordination du CNRS, 205 route de Narbonne, F-31077 Toulouse, France.*

Pablo Labra-Vázquez – *Laboratoire de Chimie de Coordination du CNRS, 205 route de Narbonne, F-31077 Toulouse, France.*

Marine Tassé – *Laboratoire de Chimie de Coordination du CNRS, 205 route de Narbonne, F-31077 Toulouse, France.*

Sonia Mallet-Ladeira – *Laboratoire de Chimie de Coordination du CNRS, 205 route de Narbonne, F-31077 Toulouse, France* ; and *Institut de Chimie de Toulouse (ICT, UAR 2599), 118 Route de Narbonne, 31062 Toulouse Cedex 09, France*.

REFERENCES

(1) Ignarro, L. J. *Nitric Oxide Biology and Pathobiology*, Academic Press, San Diego, **2000**.

(2) Butler, A. R.; Nicholson, R. *Life Death and Nitric Oxide*, The Royal Society of Chemistry, Cambridge, **2003**.

(3) Bonavida, B. *Nitric Oxide and Cancer: Prognosis, Prevention and Therapy*, Springer, New-York, **2010**.

(4) Carpenter, A. W.; Schoenfisch, M. H. Nitric oxide release: Part II. Therapeutic applications. *Chem. Soc. Rev.*, **2012**, *41*, 3742-3752.

(5) Ford, P. C. Photochemical delivery of nitric oxide. *Nitric Oxide*, **2013**, *34*, 56-64.

(6) Hossain, S.; Nisbett, L. M.; Boon, E. M. Discovery of Two Bacterial Nitric Oxide-Responsive Proteins and Their Roles in Bacterial Biofilm Regulation. *Acc. Chem. Res.* **2017**, *50*, 1633–1639.

(7) For recent reviews on nitric oxide delivery in biological environment, see:

(a) Poh, W. H.; Rice, S. A. Recent Developments in Nitric Oxide Donors and Delivery for Antimicrobial and Anti-Biofilm Applications. *Molecules* **2022**, *27*, 674-712.

(b) Paul, S.; Pan, S. ; Mukherjee, A. ; De, P. Nitric Oxide Releasing Delivery Platforms: Design, Detection, Biomedical Applications, and Future Possibilities. *Mol. Pharmacentics* **2021**, *18*, 3181-3205.

(8) Stepanenko, I.; Zalibera, M.; Schaniel, D.; Telser, J.; Arion, V. B. Ruthenium-nitrosyl complexes as NO-releasing molecules, potential anticancer drugs, and photoswitches based on linkage isomerism. *Dalton Trans.* **2022**, *51*, 5367-5393.

(9) (a) Fry, N. L.; Mascharak, P. K. Photoactive Ruthenium Nitrosyls as NO Donors: How To Sensitize Them toward Visible Light. *Acc. Chem. Res.* **2011**, *44*, 289-298.

(b) Rose, M. J.; Mascharak, P. K. Photoactive ruthenium nitrosyls: Effects of light and potential application as NO donors. *Coord. Chem. Rev.* **2008**, *252*, 2093-2114.

(10) Santana da Silva, R.; Galvao de Lima, R.; Machado, S. P. Design, Reactivity, and Biological Activity of Ruthenium Nitrosyl Complexes. *Adv. Inorg. Chem.* **2015**, *67*, 265-294.

(11) Ford, P. C. Polychromophoric Metal Complexes for Generating the Bioregulatory Agent Nitric Oxide by Single- and Two-Photon Excitation. *Acc. Chem. Res.*, **2008**, *41*, 190–200.

(12) For recent reports on ruthenium nitrosyl complexes with NO• releasing capabilities, see:

(a) Sharma, N.; Kumar, V.; Amilan Jose, D. A ruthenium nitrosyl complex-based highly selective colorimetric sensor for biological H2S and H2S–NO cross-talk regulated release of NO. *Dalton Trans.* **2023**, *52*(3), 675-682.

(b) Dela Rosa, L.B.; Jorolan, J. H. Electrochemical Investigations on the NO-Releasing Property of Ruthenium Nitrosyl Complex. *Asian J. Chem.* **2023**, *35*, 52-56

(c) Ferrarini, A.; Soek, R. N.; Rebecchi Rios, R.; Santana, F. S.; Campos, R. B.; da Silva, R. S.; Nunes, F. S. Structural, spectral, and photoreactivity properties of mono and polymetallated-2,2′-bipyridine ruthenium(II) complexes. *Inorg. Chim. Acta* **2022**, *533*, 120771.

Ma, F.; Zhang, T. T.; Zhang, Z. H.; Tong, H. X.; Yi, X. Y. Photorelease of nitric oxide in water-soluble diruthenium nitrosyl complexes with phosphonate substituted pyridylpyrrole. *Inorg. Chim. Acta* **2022**, *534*, 120826

(d) Cho, J.-H.; Kim, M.; You, Y.; Lee, H.-I. A new photoactivable NO-releasing {Ru−NO}6 ruthenium nitrosyl complex with a tetradentate ligand containing aniline and pyridine moieties. *Chem. Asian J.* **2022**, *17*, e202101244.

(e) Stepanenko, I.; Mizetskyi, P.; Orlowska, E.; Bucinsky, L.; Zalibera, M.; Venosova, B.; Clemancey, M.; Blondin, G.; Rapta, P.; Novitchi, G.; Schrader, W.; Schaniel, D.; Chen, Y.-S.; Lutz, M.; Telser, J.; Arion, V. B. The Ruthenium Nitrosyl Moiety in Clusters: Trinuclear Linear μ-Hydroxido Magnesium(II)-Diruthenium(II), μ3-Oxido Trinuclear Diiron(III)–

Ruthenium(II), and Tetranuclear μ4-Oxido Trigallium(III)-Ruthenium(II) Complexes. *Inorg. Chem.* **2022**, *61*, 950-967.

(f) Sharma, N.; Arjunan, P.; Marepally, S.; Jain, N.; Naziruddin, A. R.; Ghosh, A.; Mariappan, C. R.; Amilan, J. D. Photo controlled release of nitric oxide (NO) from amphiphilic and nanoscale vesicles based ruthenium nitrosyl complex: NO release and cytotoxicity studies. *J. Photochem. Photobiol. A* **2022**, *425*, 113703.

(g) Mikhailov, A. A.; Kostin, G. A.; Schaniel, D. The influence of the trans-ligand to NO on the thermal stability of the photoinduced side-bond coordinated linkage isomer. *New J. Chem.* **2022**, *46*(26), 12641-12650.

(h) Wu, Y.; Wang, Y.; Sun, Y.; Li, Z.; Li, X.; Zhou, Z.; Tang, D. Dissociation of Bipyridine and Coordination with Nitrosyl: Cyclometalated Ruthenium Nitrosyl Complex. *Inorg. Chem.* **2022**, *61*(24), 8997-9011.

(i) Singh, S.; Navale, G. R.; Mahale, M.; Chaudhary, V. K.; Kodam, K.; Ghosh, K. Photodissociation of nitric oxide from designed ruthenium nitrosyl complex: Studies on wound healing and antibacterial activity. *Nitric Oxide* **2022**, *129*, 30-40.

(13) Hamblin, M. R.; Demidova, T. N. Mechanisms of low level light therapy. *Proc. SPIE, Mechanism for Low-Light Therapy* **2006**, 6140, 614001–614012.

(14) Strehmel, B.; Strehmel, V. Two-Photon Physical, Organic, and Polymer Chemistry: Theory, Techniques, Chromophore Design, and Applications. *Adv. Photochem.*, **2007**, *29*, 111-341.

(15) Pawlicki, M.; Collins, H. A.; Denning, R. G.; Anderson, H. L. Two-Photon Absorption and the Design of Two-Photon Dyes. *Angew. Chem. Int. Ed.*, **2009**, *48*, 3244-3266.

(16) Juarez-Martinez, Y.; Labra-Vázquez, P.; Enríquez-Cabrera, A.; Leon-Rojas, A. F.; Martínez-Bourget, D.; Lacroix, P. G.; Tassé, M.; Mallet-Ladeira, S.; Farfán, N.; Santillan, R.; Ramos-Ortiz, G.; Malval, J.-P.; Malfant, I. Bimetallic Ruthenium Nitrosyl Complexes with Enhanced Two-Photon Absorption Properties for Nitric Oxide Delivery. *Chem. Eur. J.* **2022**, *28*, e202201692 (1-14).

(17) Lacroix, P. G.; Malfant, I.; Labra-Vázquez, P.; Farfan, N.; Ramos-Ortiz, G. Two-photon absorption-based delivery of nitric oxide from ruthenium nitrosyl complexes. *Dalton Trans.* **2022**, *51*, 14833-14841.

(18) Barzoukas, M.; Blanchard-Desce, M. Molecular engineering of push–pull dipolar and quadrupolar molecules for two-photon absorption: A multivalence-bond states approach. *J. Chem. Phys.* **2000**, *113*, 3951-3959.

(19) Zhang, X. B.; Feng, J. K.; Ren, A. M.; Sun, C. C. Theoretical Study of Two-Photon Absorption Properties of a Series of Ferrocene-Based Chromophores *J. Phys. Chem.* **2006**, 110, 12222-12230.

(20) (a) deBoer, T. R.; Mascharak, P. K. Recent Progress in Photoinduced NO Delivery With Designed Ruthenium Nitrosyl Complexes *Adv. Inorg. Chem.* **2015**, *67*, 145-170.

(b) Fry, N. L.; Mascharak, P. K. Photolability of NO in designed metal nitrosyls with carboxamido-N donors: a theoretical attempt to unravel the mechanism. *Dalton Trans.* **2012**, *41*, 4726-4735.

(c) Fry, N. L.; Wei, J.; Mascharak, P. K. Triggered Dye Release via Photodissociation of Nitric Oxide from Designed Ruthenium Nitrosyls: Turn-ON Fluorescence Signaling of Nitric Oxide Delivery. *Inorg. Chem.* **2011**, *50*, 9045-9052.

(d) Fry, N. L.; Rose, M. J.; Rogow, D. L.; Nyitray, C.; Kaur, M.; Mascharak, P. K. Ruthenium Nitrosyls Derived from Tetradentate Ligands Containing Carboxamido-N and Phenolato-O Donors: Syntheses, Structures, Photolability, and Time Dependent Density Functional Theory Studies. *Inorg. Chem.* **2010**, *49*, 1487-1495.

(21) (a) Roose, M.; Sasaki, I.; Bukhanko, V.; Mallet-Ladeira, S.; Barba-Barba, R. M.; Ramos-Ortiz, G.; Enriquez-Cabrera, A.; Farfán, N.; Lacroix, P. G.; Malfant, I. Nitric oxide photo-release from a ruthenium nitrosyl complex with a 4,4′-bisfluorenyl-2,2′-bipyridine ligand. *Polyhedron* **2018**, *151*, 100-111.

(b) Bukhanko, V.; Lacroix, P. G.; Sasaki, I.; Tassé, M.; Mallet-Ladeira, S.; Voitenko, Z.; Malfant, I. Mechanism and oxidation state involved in the nitric oxide (NO) photorelease in a

terpyridine-bipyridine-based ruthenium nitrosyl complex. *Inorg. Chim. Acta* **2018**, *482*, 195-205.

(c) Roose, M.; Tassé, M.; Lacroix, P. G.; Malfant, I. Nitric oxide (NO) photo-release in a series of ruthenium–nitrosyl complexes: new experimental insights in the search for a comprehensive mechanism. *New J. Chem.* **2019**, *43*, 755-767.

(d) Romero-Ávila, M.; León Rojas, A. F.; Lacroix, P. G.; Malfant, I.; Farfan, N.; Mhanna, R.; Santillan, R.; Ramos-Ortiz, G.; Malval, J.-P. Two-Photon-Triggered NO Release via a Ruthenium–Nitrosyl Complex with a Star-Shaped Architecture. *J. Phys. Chem. Lett.* **2020**, *11*, 6487-6491.

(22) Dixneuf, P. H. Activation of alkynes with ruthenium complexes. *Pure & App. Chem.* **1989**, *61*, 1763-1770.

(23) Boulton, L. Sonogashira Coupling. in Synthetic Methods in Drug Discovery: Volume 1, ed. Blakemore, D. C; Doyle, P. M.; Fobian, Y. M.; Blakemore, D.; Fobian, Y.; Doyle, P. The Royal Society of Chemistry, **2016**, vol. 1, ch. 4, pp122-142.

(24) Mingos, D. M. P. Nitrosyl Complexes in Inorganic Chemistry, Biochemistry and Medicine I (Ed.: Mingos, D. M. P.), Springer Berlin Heidelberg, Berlin, Heidelberg, **2014**, pp. 1-44.

(25) (a) Bukhanko, V.; León-Rojas, A. F.; Lacroix, P. G.; Tassé, M.; Ramos-Ortiz, G.; Barba-Barba, R. M.; Farfán, N.; Santillan, R.; Malfant, I. Two-Photon Absorption Properties in "Push-Pull" Ruthenium Nitrosyl Complexes with various Fluorenylterpyridine-Based Ligands. *Eur. J. Inorg. Chem.* **2021**, 1670-1684.

(b) Labra-Vázquez, P.; Bocé, M.; Tassé, M.; Mallet-Ladeira, S.; Lacroix, P. G.; Farfán, N.; Malfant, I. Chemical and photochemical behavior of ruthenium nitrosyl complexes with terpyridine ligands in aqueous media. *Dalton Trans.* **2020**, *49*, 3138-3154.

(26) Pimienta, V.; Levy, G.; Lavabre, D.; Samat, A.; Guglielmetti, R.; and Micheau, J.C. Kinetic analysis of photochromic systems under continuous irradiation: Application to spiropyrans. *J. Phys. Chem.* **1996**, *100*, 4485-90.

(27) Marcolongo, J. P.; Schmidt, J.; Levon, N.; Slep, L. D. A chemometric approach for determining the reaction quantum yields in consecutive photochemical processes. *Phys. Chem. Chem. Phys.* **2017**, 19, 21373-21381.

(28) see for example:

(a) Klausen, M.; Blanchard-Desce, M. Two-photon uncaging of bioactive compounds: Starter guide to an efficient IR light switch. *J. Photochem. Photobiol. C: Photochem. Rev.* **2021**, *48*, pp.100423.

(b) Pálfi, D.; Chiovini, B. ; Szalay, G.; Kaszás, A.; Turi, G. F.; Katona, G.; Ábrányi-Balogh, P.; Szőri, M.; Potor, A.; Frigyesi, O.; Haveland, C. L.; Szadai, Z.; Madarász, M.; Vasanits-Zsigrai, A.; Molnár-Perl, I.; Viskolcz, B.; Csizmadia, I. G.; Mucsi, Z.; Rózsa, B. High efficiency two-photon uncaging coupled by the correction of spontaneous hydrolysis. *Org. Biomol. Chem.* **2018**, *16*, 1958-1970.

(c) Piant, S.; Bolze, F.; Specht, A. Two-photon uncaging, from neuroscience to materials. *Opt. Mater. Express* **2016**, *6*, 1679-1691.

(d) Bolze, F.; Nicoud, J.-F.; Bourgogne, C.; Gug, S.; Sun, X. H.; Goeldner, M.; Specht, A.; Donato, L.; Warther, D.; Turi, G. F.; Losonczy, A. Two-photon uncaging: The chemist point of view. *Opt. Mater.* **2012**, *34*, 1664-1669.

(29) Pimienta, V.; Lavabre, D.; Micheau, J. C. (https://cinet.chim.cnrs.fr/), together with examples and notice.

Synopsis

A two-step (A $\rightarrow$ B $\rightarrow$ C) kinetics model specially designed for bimetallic bis-nitrosyl ruthenium complexes and supported by the synthesis and the full characterization of intermediate compound and final products (photoproducts) provides a relevant description of the mechanism involved in the photorelease of nitric oxide.

Table of Contents Graphic